Applied Catalysis B: Environmental 257 (2019) 117908

Contents lists available at ScienceDirect

Applied Catalysis B: Environmental

journal homepage: www.elsevier.com/locate/apcatb

NIR light driven catalytic hydrogen generation over semiconductor photocatalyst coupling up-conversion component

Wei Gao[a,b], Bin Tian[a,b], Wenyan Zhang[c], Xuqiang Zhang[a], Yuqi Wu[a], Gongxuan Lu[a,*]

[a] State Key Laboratory for Oxo Synthesis and Selective Oxidation, Lanzhou Institute of Chemical Physics, Chinese Academy of Sciences, Lanzhou 730000, China
[b] University of Chinese Academy of Sciences, Beijing 100049, China
[c] College of Material Engineering, Jinling Institute of Technology, Nanjing, China

ARTICLE INFO

Keywords:
Infrared light induced photocatalytic overall water splitting
NIR-to-visible up-conversion
CdS catalyst
NYF upconversion component
Inhibition of hydrogen and oxygen recombination

ABSTRACT

Solar irradiation spectrum on the earth consists of about 50% infrared energy, which has not used effectively in chemical storage and conversion into hydrogen via photocatalytic route. In this work, we reported the catalytic hydrogen generation over a photocatalyst consisting of semiconductor CdS and an up-conversion component $NaYF_4$-Yb^{3+}-Er^{3+} (NYF) under infrared light irradiation. Under 980 nm laser irradiation, the input infrared light was up-converted into visible light, which was used to excite CdS to produce hydrogen and oxygen. The isotope experiments confirmed both of hydrogen and oxygen were produced from water. The highest hydrogen evolution rate of 3.38 μmol g^{-1} h^{-1} has been achieved. 0.008% of AQE under NIR light irradiation has been approached.

1. Introduction

Photocatalytic hydrogen evolution from water splitting is one of the most promising ways to store and convert the solar energy, however, to utilize the wide spectrum of sun light and to construct a stable photocatalytic system are still two remained challenging obstacles [1–9]. Sun light spectrum on the earth is consist of 5% of UV light, 46% of visible light, and 49% of infrared (IR) light, respectively. Since IR light itself accounts for nearly half of the solar spectrum, using IR irradiation driven hydrogen evolution is more important for the utilization, conversion and storage of solar energy.

Up to now, efforts of using IR light in photocatalysis are primarily focused on its thermal effect. It is known that water can be split into hydrogen and oxygen over 2500 K, which makes production of hydrogen from water via solar thermal process very inefficient [10–13]. Besides, the materials available for such high temperature operation are seldom reported [12,13]. Another option is conversion IR irradiation into electricity, and then using electricity to electrolyze water. Thanks to the progress of thermoelectric materials [14,15], coupling thermoelectric materials and electrocatalysts for hydrogen evolution already have been used in some photoelectrocatalytic systems, although the efficiency is waiting for improvement. For example, Shari et al. [14] designed two-dimensional layered thermoelectric materials Sb_2Te_3 and $Bi_{0.5}Sb_{1.5}Te_3$ as thermoelectric voltage source to initiate and boost electrocatalytic reactions.

NIR-to-visible up-conversion (UC) is another promising route of using NIR light to induce chemical reaction in solar energy conversion. It is known that UC material can convert NIR light to visible light due to the abundant 4f energy levels in rare earth atoms. The emitted up-converted energy can excite visible light-respond photocatalysts to generate electrons and holes and initiate water splitting. More recently, some efforts already have been devoted onto this process [16,17]. For example, Guo et al. [16] reported a $NaYF_4$-Yb-Tm/CdS/TiO_2 photocatalyst for degradation of methylene blue in aqueous solution upon NIR irradiation. Feng et al. [17] constructed a sandwich-structured $NaYF_4$-Yb^{3+}-Er^{3+}/Au/CdS architecture, using the UC property and the surface plasmon resonance of Au, realizing hydrogen production through photoreforming of renewable bio-ethanol. It is probable to design a catalyst active for water splitting under IR irradiation based on coupling NIR-to-visible up-conversion materials with visible light sensitive semiconductor [18–31].

$NaYF_4$-Yb^{3+}-Er^{3+} (NYF) is one of the most efficient NIR to visible up-converters (UC) due to its near-perfect resonance between a specific crystal-field level of Yb^{3+} and Er^{3+} [26,27]. UC can also take place through direct (resonant) energy transfer from Yb^{3+} to Er^{3+} [28]. The NIR-to-visible UC process in $NaYF_4$-Yb^{3+}-Er^{3+} is mainly attributed to the energy transfer UC (ETU) process between Yb^{3+} and Er^{3+} ions in $NaYF_4$ lattices, as illustrated in Scheme 1 [16,17,26,28]. Under excitation of lower energy photons (~976 nm), both the sensitizer (Yb^{3+}) and the activator (Er^{3+}) could be pumped to their excited states.

* Corresponding author.
E-mail address: gxlu@lzb.ac.cn (G. Lu).

https://doi.org/10.1016/j.apcatb.2019.117908
Received 19 March 2019; Received in revised form 17 June 2019; Accepted 27 June 2019
Available online 29 June 2019

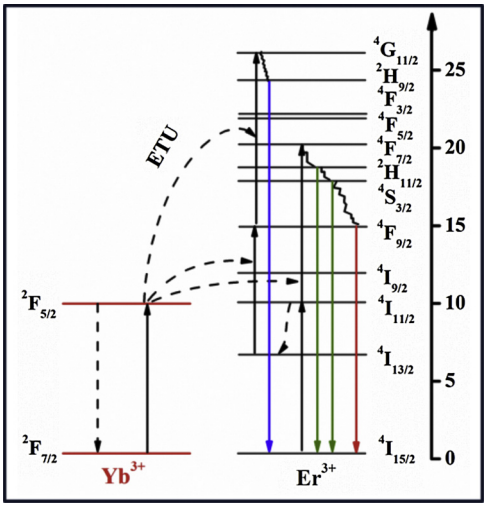

Scheme 1. Up-conversion mechanism of Yb^{3+} and Er^{3+} in $NaYF_4$ lattice.

Subsequently, the non-radioactive sensitizer donates the energy to the activator via a dipole-dipole resonant interaction (Yb^{3+}: $^2F_{5/2} \rightarrow Er^{3+}$: $^4I_{11/2}$), one Yb^{3+} ion transfers back to the ground state, the Er^{3+} ion transfers to a state of higher energy simultaneously. Due to the energy level match, the Er^{3+} ions can be populated to their higher excited states via a similar resonant energy transfer from the sensitizers ($^4I_{11/2} \rightarrow {}^4F_{7/2}$ or $^4I_{13/2} \rightarrow {}^4F_{9/2}$). The multi-excited Er^{3+} ions relax non-radioactively to the $^2H_{11/2}$ and $^4S_{3/2}$ states, generating green emissions. De-excitation of the $^4F_{9/2}$ state from higher energy levels or resonant energy transfer from $^4I_{13/2}$, results in red emissions via a $^4F_{9/2} \rightarrow {}^4I_{15/2}$ transition [26,28], providing green and red light emission. Since the energy gap between Yb^{3+}: $^2F_{7/2} \rightarrow {}^2F_{5/2}$ corresponds to the irradiation about 976 nm, the $NaYF_4$-Yb^{3+}-Er^{3+} can absorb near-infrared light, therefore, the energy transfer between Yb^{3+} and Er^{3+} result in the NIR-to-visible energy up-conversion eventually. If $NaYF_4$-Yb^{3+}-Er^{3+} is coupled with CdS, an excellent visible-light response semiconductor catalyst [32–42], IR driven water splitting is possible.

Since water splitting to hydrogen is also impeded by the reverse reaction of the recombination of hydrogen and oxygen over the co-catalysts and photocatalysts [43–46], and the dissolved amount of oxygen in water is about 3 times (mole ratio) higher than that of hydrogen in water, the nascent formed oxygen likes dissolve in water instead of escape to gas phase, which leads to kinetic advantage of the reverse reaction of hydrogen and oxygen recombination over the photocatalysts when hydrogen is formed. Therefore, hydrogen generation reaction composition must contain a component which can combine oxygen in suitable state to prevent its activation on catalyst surface. Perfluorodecalin (PFDL), a derivative of decalin in which all of the hydrogen atoms are replaced by fluorine atoms, is one of right candidates for this purpose. PFDL has an ability of dissolving huge amount of oxygen (16 mL of PFDL can dissolve 0.12 mg of oxygen at standard conditions of normal temperature and pressure, see Fig. S1), which can decrease the oxygen concentration over catalyst surface and prevent the reverse reaction of hydrogen and oxygen recombination effectively.

In this work, we developed a catalyst, consisting of CdS/Pt and upconversion component $NaYF_4$-Yb^{3+}- Er^{3+}, and fulfilled water splitting to hydrogen and oxygen under 980 nm NIR illumination. The hydrogen generation rate of 3.38 μmol g^{-1} h^{-1} has been achieved and satisfied stability has been accomplished.

2. Experimental section

2.1. Synthesis of CdS

CdS sample was synthesized via a precipitation method. Typically, 3.70 g $Cd(NO_3)_2{\cdot}4H_2O$ was dissolved in 200 mL deionized water and stirred vigorously for 1 h, 6.68 g $Na_2S{\cdot}9H_2O$ was dissolved into another 80 mL deionized water to obtain Na_2S solution by ultrasonic treatment. Then the Na_2S solution was slowly added into the $Cd(NO_3)_2$ solution drop-by-drop under vigorous stirring. After stirring for 3 h, kept the solution overnight at room temperature, the yellow precipitate was obtained, filtrated, and washed with deionized water several times, then dried at 60 °C for 12 h. Finally, the products were collected and grounded into powder by an agate mortar.

2.2. Synthesis of NYF and CdS/NYF

The $NaYF_4$-Yb^{3+}-Er^{3+} was synthesized via a modified one step hydrothermal method [16]. Briefly, 1.41 mmol of $Y(NO_3)_3$, 0.16 mmol of $Yb(NO_3)_3$ and 0.032 mmol of $Er(NO_3)_3$ were dissolved into 20 mL of deionized water and named solution A. 14.4 mmol of NaF was added into another 20 mL of deionized water forming solution B. The solution A and B were heated to 60 °C then added B to A drop-by-drop under stirring. The obtained mixture was continuously stirred at 60 °C for another 1 h. The final solution was transferred into a 100 mL Teflon lined autoclave and heated at 180 °C for 3 h. After cooling to room temperature, the obtained precipitate was collected by centrifugation, was washed with deionized water and absolute ethanol several times, and then was dried at 60 °C overnight.

For CdS/NYF synthesis, another portion of solution C was prepared by dispersing different amount of CdS (0.1, 0.15, 0.2, 0.25 and 0.3 g, which corresponding to the weight percentages of NYF at 29%, 32%, 40%, 47% and 55%) into 20 mL water. Added A and B in order into solution C dropwise and under stirring, 0.5 h of stirring time was needed before adding B. The mixture continuously was stirred for another 1 h and all the operations were carried out under the temperature of 60 °C. The subsequent hydrothermal steps were similar as described above.

2.3. Synthesis of Pt/CdS/NYF, CdS/Pt and NYF/Pt

The Pt/CdS/NYF was prepared by a typical hydrazine hydrate reduction method. 0.20 g as-prepared CdS/NYF sample with a calculated amount of K_2PtCl_6 solution (the weight ratio of Pt to CdS/NYF was 2 wt %) was stirred for half an hour, then hydrazine hydrate was added into the solution. When the reduction was finished, the products were filtrated, rinsed with deionized water, and dried at 60 °C to obtain the Pt/CdS/NYF photocatalysts. The same method was used to synthesize CdS/Pt and NYF/Pt.

2.4. Photocatalytic H_2 evolution activity

Photocatalytic reactions were carried out in a sealed pyrex flask (190 mL), which has a flat window with the irradiation area about 14 cm^2 at room temperature. In a typical reaction, 50 mg Pt/CdS/NYF and 1 mL PFDL were dispersed into 140 mL distilled water in a sealed pyrex flask. The mixture was ultrasonic treated 30 min before bubbling Ar gas to degas for 30 min, subsequently the reactor was irradiated under 420 nm, 980 nm and NIR light respectively. During the process, the gas composition in the sealed Pyrex flask was monitored by gas chromatography. The photocatalyst activity of hydrogen evolution was measured with gas chromatography (Agilent 6820, TCD, 13 × column, Ar carrier). The light source was a 300-W Xenon lamp with a denoted cutoff filter and a 2.8-W 980 nm laser (NBET-980-3). For comparison, some reaction systems have no PFDL.

The hydrogen recombination reactions were studied by injection of 0.5 mL H_2 and O_2 in reaction system before illumination. The blank experiments were taken in the absence/presence of PFDL to confirm the function of PFDL.

The hydrogen evolution reactions under different temperatures (40, 50, 60, 70, 80, 90 °C respectively) under dark were conducted, in which

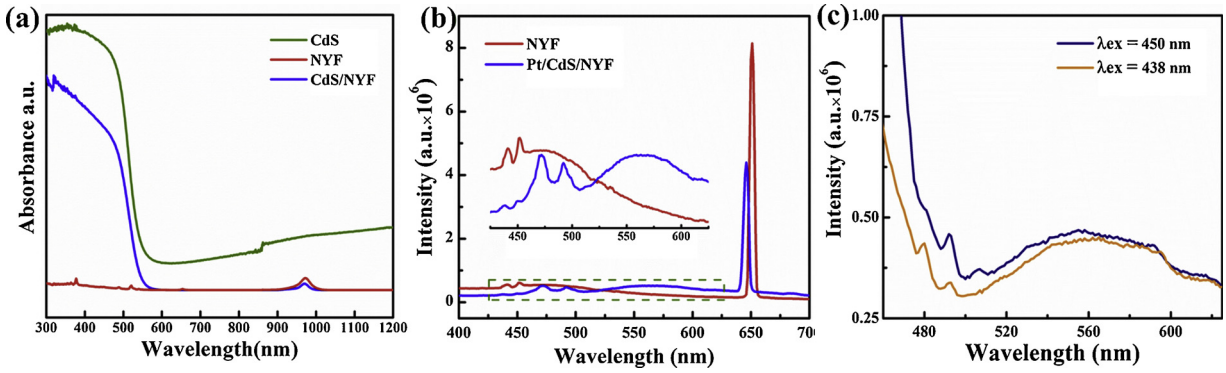

Fig. 1. (a) The UV–vis-NIR absorption spectra of CdS, NYF and CdS/NYF. (b) The photoluminescence (PL) spectra of the NYF and Pt/CdS/NYF under 980 nm excitation (inset: the magnified emission spectra of NYF and Pt/CdS/NYF during 425 ~ 625 nm). (c) The photoluminescence (PL) spectra of CdS under 438 and 450 nm excitation.

the reactor was put in a water bath at different temperatures.

2.5. Isotopes tracer experiments

In order to confirm the overall water splitting to hydrogen and oxygen simultaneously over Pt/CdS/NYF photocatalyst, isotopes tracer experiments were carried out. Experimental steps were followed by the method described above, except the distilled water was changed to D_2O (CAS:7789-20-0, the purity of D is 99.9 atom%) or $H_2{}^{18}O$ (CAS:14314-42-2, the purity of ^{18}O is 90 atom%) for the detection of D_2 and $^{18}O_2$. The formed D_2 and $^{18}O_2$ were measured by GC–MS (TILON-LC-D200 M).

2.6. Photoelectrochemical measurements

All the photoelectrochemical measurements were carried out on an electrochemical analyzer (CHI660E) in a homemade standard three-electrode cell, consisting of an organic glass enclosure with a quartz window and a 1.2 cm diameter opening opposite the window to the work electrode clamped. The working electrodes were prepared by dropping the catalyst sample directly onto the surface of the precleaned indium tin oxide glass (ITO glass). The area of the working electrode exposed to the electrolyte was about 1 cm^2. Platinum foil was used as counter electrode and a saturated calomel electrode (SCE) as the reference electrode. The current-time curve was obtained under unbiased condition to investigate the anodic photocurrent. The linear sweep voltammetry (LSV) curves were recorded with the scan rate of 0.5 mVs^{-1}. The excitation source was a 300-W Xenon lamp with the 420 nm cut-off filter, 550 nm, 630 nm and NIR light bandpass filters respectively. The electrolyte was 0.1 M Na_2SO_4 solution.

The apparent quantum efficiency (AQE) was measured under the same photocatalytic reaction conditions with irradiation light through a bandpass filter (490, 520, 550, 630 nm and NIR light). Photon flux of the incident light was determined using a Ray virtual radiation actinometer (FU 100, silicon ray detector, light spectrum, 400–700 nm; sensitivity, 10–50 μV μm mol^{-1} $m^{-2}s^{-1}$). The reaction solutions were irradiated for 2 h with bandpass filters for AQE tests of the H_2 production. The following equation was used to calculate the AQE.

AQE = 2× the number of evolved hydrogen molecules/the number of incident photos × 100%

The calculation of laser energy to hydrogen (LTH) conversion efficiency

LTH = (Energy of generation of hydrogen by water splitting) / (Laser energy irradiating the reaction cell) = E_H/E_{Laser}

$E_H = n \times 6.02 \times 10^{23} \times 2.46 \times 1.609 \times 10^{-19}$, n is the amount of hydrogen during reaction time ($mol{\cdot}h^{-1}$), 2.46 eV is the free energy of water splitting.

E_{Laser} = P × t, P is the power of laser (2.8 W), t is the reaction time (1 h).

2.7. Characterizations of the catalysts

The X-ray diffraction patterns (XRD) of the samples were recorded on a Rigaku B/Max-RB X-ray diffractometer with a nickel-filtrated Cu Kα radiation, specifically using a position sensitive detector at the step time of 15 s at 40 mA and 40 kV, scan step 0.017°, and the 2θ range was 5–90°. X-ray photoelectron spectroscopy (XPS) analysis was conducted with a VG Scientific ESCALAB210-XPS photoelectron spectrometer with an Al Kα X-ray resource. Transmission electron microscopy (TEM) and HRTEM images were obtained using a Tecnai-G2-F30 field emission transmission electron microscope operating at accelerating voltage of 300 kV. The fluorescence spectra were measured using a Hitachi F-4500 fluorescence spectrometer with excitation wavelength at 970 nm respectively. Ultraviolet-visible (UV–vis) diffuse reflectance spectra (DRS) were obtained with a PerkinElmer Lambda 950 UV/VIS/NIR spectrometer in which $BaSO_4$ powder was used as the internal standard to obtain the optical properties of the samples.

3. Results and discussions

3.1. Up-conversion property of $NaYF_4$-Yb^{3+}-Er^{3+} and CdS/$NaYF_4$-Yb^{3+}-Er^{3+}

The optical absorption properties of the as-prepared samples were studied by UV–vis-NIR absorption spectroscopy and photoluminescence spectroscopy. As shown in Fig. 1(a), the NYF exhibits the absorption around 975 nm. The obtained catalyst shows NIR absorption in NIR region and shows better light response in visible-NIR region than CdS itself. The clear blue (~420 nm), green (~550 nm) and red light (~650 nm) can be emitted by taking advantage of up-conversion process of $NaYF_4$-Yb^{3+}-Er^{3+} under NIR light irradiation [16,26–28]. According to the result shown in Fig. 1(b), the NYF gives obvious emission peak around 650 nm and relative weak emission peaks around 450 nm under 975 nm excitation. The up-converted energy around 450 nm can excite CdS generate electrons and holes for water splitting (Fig. 1(c)). The NIR-to-visible UC process of NYF was also investigated by transient photocurrent test. As results shown in Fig. 2(a) and (b), CdS/Pt does not exhibit photo-current under NIR light irradiation. When the CdS/Pt is assembled with NYF, Pt/CdS/NYF exhibit obviously enlarged photocurrent under NIR light irradiation, which confirms that the incident NIR light is converted to visible light by NYF to yield large amounts of photogenerated charges in CdS. In order to check activity of Pt/CdS/NYF for water splitting, the 980 nm laser was used as well (shown in Picture 1). Green light was emitted from NYF and Pt/CdS/NYF solution under 980 nm laser irradiation correspondingly.

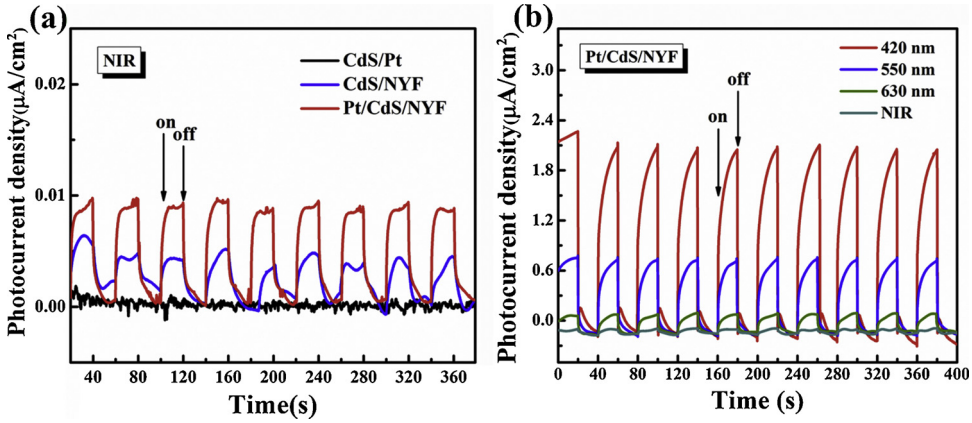

Fig. 2. (a) Transient photocurrent-time curves of CdS/Pt, CdS/NYF and Pt/CdS/NYF under NIR light; (b) Transient photocurrent-time curves of Pt/CdS/NYF under 420 (cut-off filter), 550, 630 nm and NIR light (bandpass filters).

3.2. Photocatalytic water splitting over CdS/Pt and Pt/CdS/NYF photocatalysts

Based on the NIR-to-visible up-conversion properties of NYF and Pt/CdS/NYF, photocatalytic water splitting reactions were carried out over CdS/Pt and Pt/CdS/NYF. Since the nascent formed H_2 and O_2 might recombined over Pt via reverse reaction of hydrogen and oxygen [47], PFDL was used to combine the nascent formed oxygen to prevent it activation over catalyst surface. The role of PFDL has been reported in the previous references [47–50] (see Figs. S1, S2 and 3 (a)). The concentration of hydrogen in the reactor decrease very significantly in the absence of PFDL, which indicated that the newly formed hydrogen would react with dissolved oxygen in water.

LSV tests show that the Pt/CdS/NYF photocatalysts exhibit lower hydrogen evolution potential than CdS and CdS/NYF (Fig. 3(b)), indicating that hydrogen are more liable to be generated over Pt/CdS/NYF catalyst. The recombination rates over Pt/CdS/NYF significantly decreased in the presence of PFDL (Fig. 3(a)). Thereafter, the HER were effectively promoted over the Pt/CdS/NYF photocatalyst and NIR-light-driven overall splitting water achieved (Fig. 3(c)).

Photocatalytic hydrogen evolution reactions were investigated and results were shown in Fig. 4. CdS/Pt itself cannot generate hydrogen under NIR light irradiation, however, Pt/CdS/NYF generates significant amount of hydrogen under 980 nm laser light and NIR light (800nm~1600 nm) irradiation, indicating that the hydrogen evolution activity under NIR light is mainly derived from the up-conversion contribution of NYF (Fig. 4(a)). The highest H_2 evolution rate of 3.38 μmol g^{-1} h^{-1} is achieved over Pt/CdS/NYF photocatalyst under 980 nm laser light irradiation with 40 wt % NYF. And the corresponding laser energy-to-hydrogen conversion efficiency (LTH) is 0.008%. Hydrogen evolution reactions under different temperatures without irradiation (under dark) also were studied to eliminate the effect of temperature. No hydrogen was detected until the temperature reached 90 °C, the corresponding hydrogen detected was about 0.33 μmol g^{-1} after one hour heating (Fig. S3), which was much lower than that under 980 nm laser irradiation. Therefore, it is infrared light, rather than heat, inducing photocatalytic hydrogen production from water under 980 nm laser irradiation. The AQEs of Pt/CdS/NYF for hydrogen evolution were also measured under 490, 520, 550, 630 nm and NIR light respectively (see Fig. 4(b)). 0.008% of AQE under NIR light irradiation was achieved. The corresponding hydrogen evolution rate is 0.68 μmol g^{-1} h^{-1} (Fig. S4). Besides, Pt/CdS/NYF shows a higher activity and stability than CdS/Pt under $\lambda \geq 420$ nm light irradiation (Fig. 4(c)) and maintained its stability under NIR light irradiation over 15 h (Fig. 3(c)). According to the reference data shown in Table S1, our catalyst (Pt/CdS/$NaYF_4$-Yb^{3+}-Er^{3+}) is the first example for overall water splitting without sacrificial reagent addition under 980 nm irradiation. Furthermore, we tested activities of different samples with various percentages of $NaYF_4$-Yb^{3+}-Er^{3+} in the Pt/CdS/NYF photocatalysts under visible light irradiation, as the results shown in Fig. 4(d), the best photocatalytic activity could be obtained over 40% NYF in catalyst.

Isotopes tracer experiments were conducted to confirm NIR-light-driven water splitting to hydrogen and oxygen. As results shown in Fig. 5, D_2 and $^{18}O_2$ were detected when D_2O and $H_2{}^{18}O$ were used as reactants respectively. These results prove that the H_2 and O_2 are generated from photocatalytic water splitting. Given that the purity of $H_2{}^{18}O$ was 90 atom% ^{18}O, isotopic exchange would occur during the

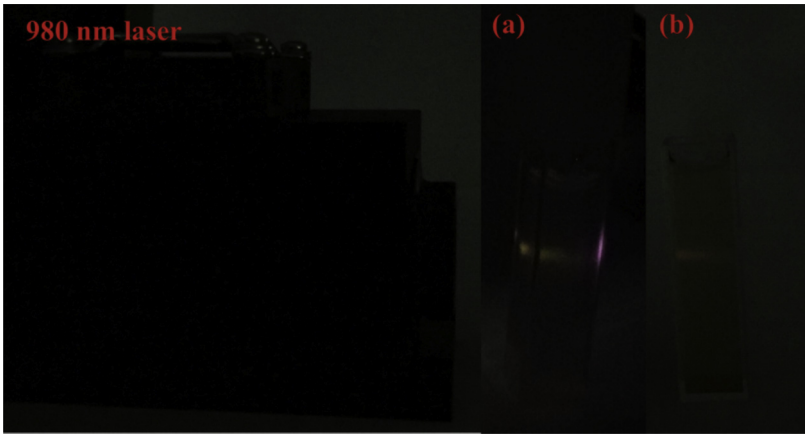

Picture 1. The photos of (a) NYF and (b) Pt/CdS/NYF under 980 nm laser irradiation.

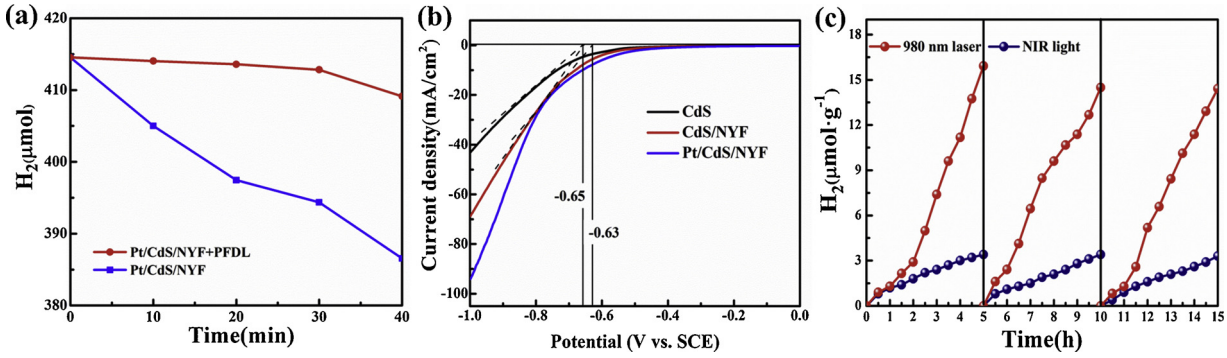

Fig. 3. (a) Hydrogen recombination reaction curves over Pt/CdS/NYF with and without PFDL. (b) LSV curves of CdS, CdS/NYF and Pt/CdS/NYF photocatslysts on ITO glass. The electrolyte was 0.1 M Na_2SO_4 solution. (c) Stability testing of Pt/CdS/NYF with PFDL over 980 nm laser and NIR light irradiation.

splitting of $H_2{}^{18}O$ and $H_2{}^{16}O$, consequently, $^{18}O_2$, $^{16}O^{18}O$ and $^{16}O_2$ were also detected simultaneously. We also measured the ratio of hydrogen and oxygen formed during reaction, and the results was given in Table S2. The results were closed to 2:1 in long-term runs.

3.3. Characterization of $NaYF_4$-Yb^{3+}-Er^{3+} and Pt/CdS/$NaYF_4$-Yb^{3+}-Er^{3+}

More detailed investigation was conducted to reveal more intrinsic relationship between the structure of Pt/CdS/NYF photocatalyst and its high efficiency for NIR-light-driven water splitting. The transmission electron microscopy and energy dispersive spectrometry are shown in Fig. 6, and additional HRTEM spectra are shown in Fig. S5. It is clear that CdS particles are anchored on the surface of NYF. The HRTEM in Fig. 6(d) shows the lattice structure of Pt/CdS/NYF, in which an interlayer spacing of 0.335 nm can be ascribed to the (111) plane of cubic CdS. The interlayer spacing of 0.311 nm can be assigned to the (111) plane of NYF. The interlayer spacing of 0.227 nm is belonged to (111) plane of Pt nanoparticle. Catalyst components are in good match state. Average particle size of Pt was calculated from a fairly large number of particles in HRTEM images and the mean value was 2.31 nm (noted by histogram in Fig. S6). The element mapping and EDX spectrum of Pt/CdS/NYF in Fig. 6(e) and (f) illustrate that all the elements distribute homogeneously in Pt/CdS/NYF catalyst, indicating the CdS disperse uniformly on the surface of NYF to form large areas of CdS/NYF heterojunctions, through which could the energy and carrier be transferred effectively between them. Consequently, the visible light generated by NYF could be better used by CdS for splitting water.

XRD patterns show the typical peaks of NYF (JCPDS#77-2042) [51] and CdS (JCPDS#80-0019) [52] in Pt/CdS/NYF photocatalyst (see Fig. 7(a)). A left-shoulder of the CdS-(111)-reflection appears when CdS combines with NYF (Figs. 7(a) and S7). Hydrothermal (180 °C) process resulted in the crystal phase transition of CdS (cubic → hexagonal) [53,54], the weak peak around 25° can be attributed to (100) facet crystal plane of hexagonal CdS. The survey XPS of Pt/CdS/NYF catalyst indicate typical peaks of Cd, S, Na, F, Y, Er, Yb and Pt signals (Fig. 7(b)). Both Er and Yb binding energies imply that Er and Yb mainly exist in Er^{3+}/Yb^{3+} chemical states [55], which are necessary for the NIR-to-visible UC in NYF lattices (Fig. 8(a) and (b)). It is seen that the binding energy of Pt ($4f_{7/2}$) in Pt/CdS/NYF is 72.28 eV in the metallic state (Fig. 8(c)) and Pt particles expose the high-energy (111) planes in Pt/CdS/NYF (Fig. 6(c)). The metallic Pt NPs are capable of hydrogen

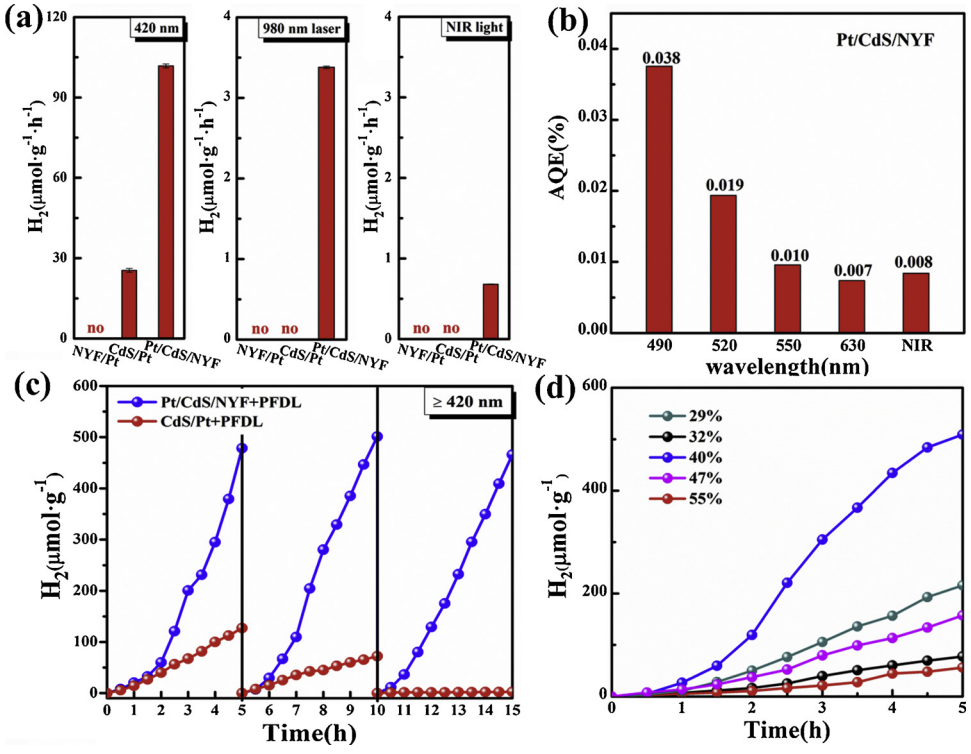

Fig. 4. (a) Photocatalytic activity of NYF/Pt, CdS/Pt and Pt/CdS/NYF under NIR light (800 ~ 1600 nm band pass filter) and λ ≥ 420 nm (cut-off filter); (b) The AQEs of Pt/CdS/NYF; (c) Stability tests of Pt/CdS/NYF and CdS/Pt over 420 nm light; (d) Photocatalytic activities over Pt/CdS/NYF with the different weight percentages of NYF under visible light irradiation (λ ≥ 420 nm).

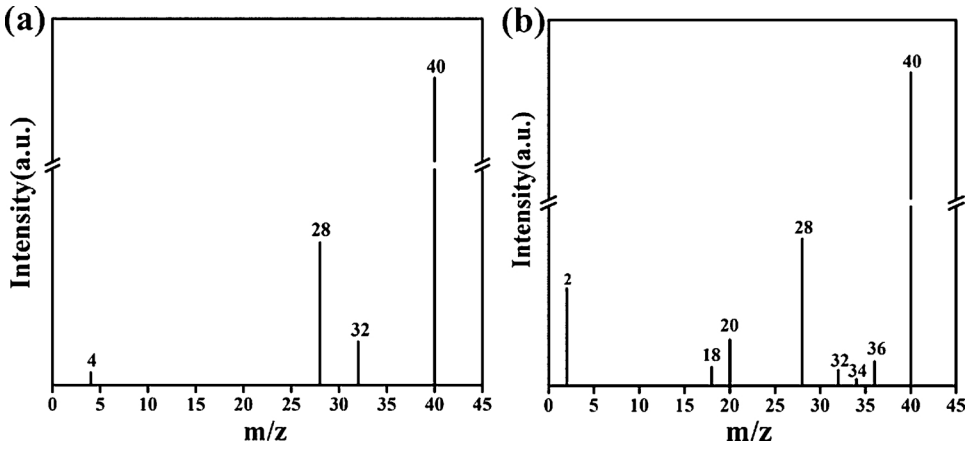

Fig. 5. GC–MS spectra of water splitting gas products in the presence of (a) D_2O and (b) $H_2{}^{18}O$.

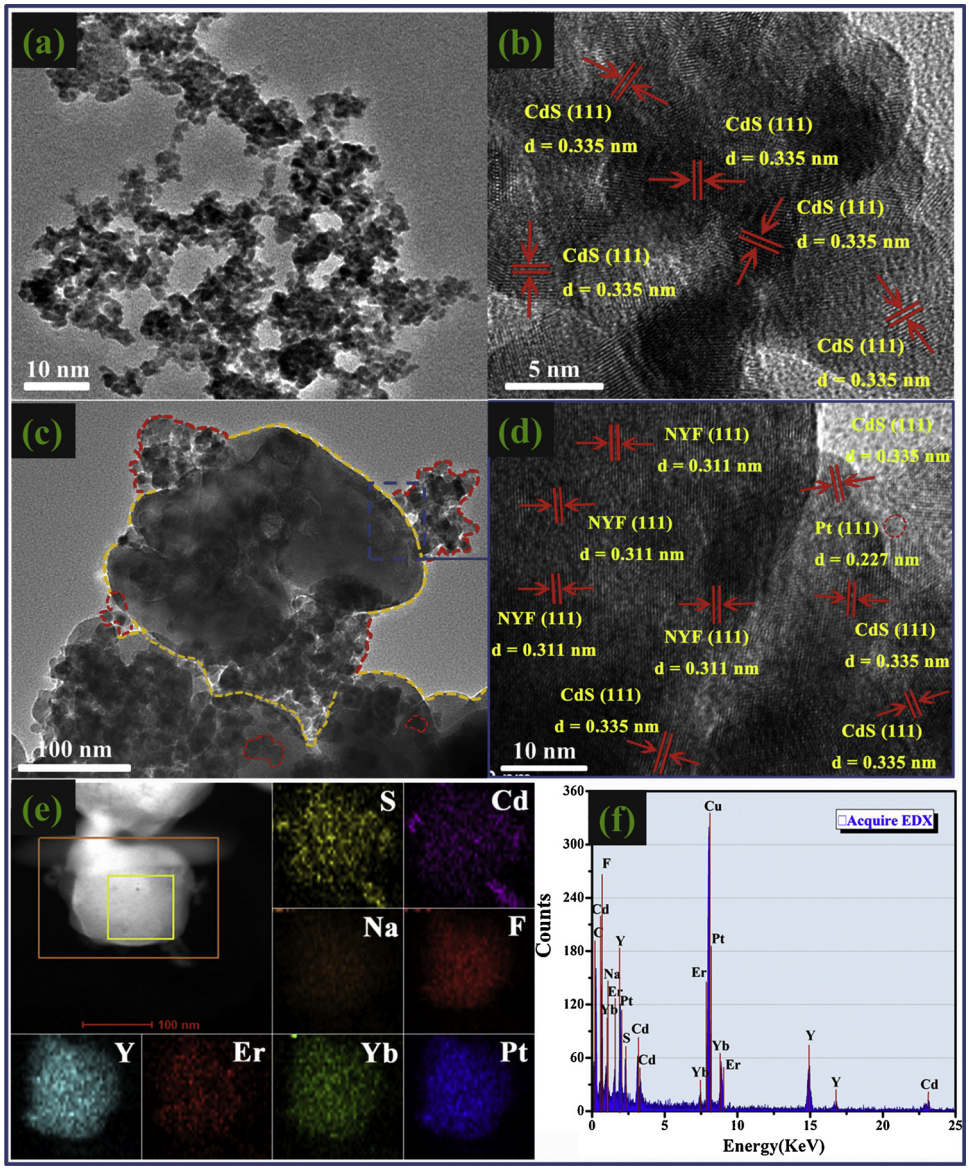

Fig. 6. (a)TEM and (b) HRTEM images of CdS; (c)TEM and (d) HRTEM images of Pt/CdS/NYF; (e) Element mapping images and (f) EDX spectrum of Pt/CdS/NYF ((e) and (f) are came from the region of orange rectangle).

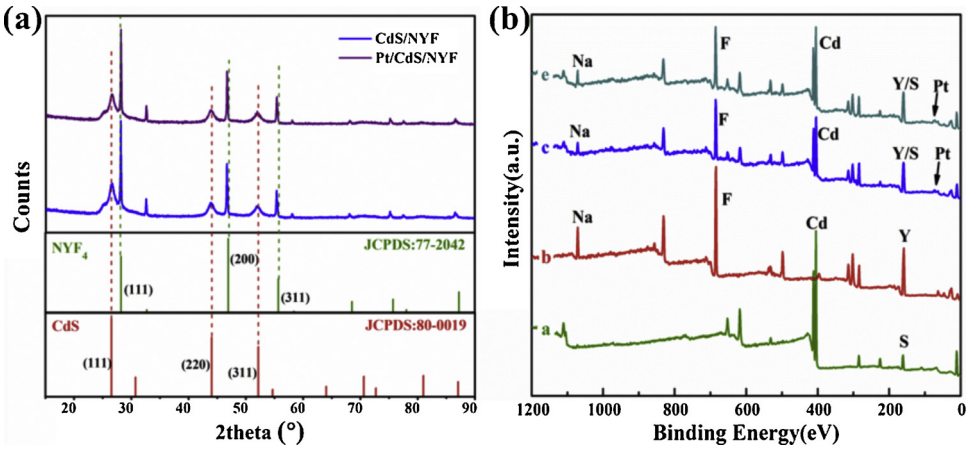

Fig. 7. (a) XRD patterns of CdS/NYF and Pt/CdS/NYF; (b) XPS survey of a-CdS, b-NYF, c-Pt/CdS/NYF before and d-Pt/CdS/NYF after reaction.

evolution site which offer lower the HER over-potential for hydrogen generation. In addition, the heterojunctions between CdS and NYF led to high binding energy shift of S 2p and Na 1 s (Fig. 9). It is worth noting that, the binding energy of S 2p is close to Y 3d, (Y $3d_{5/2}$ (159.5, 195.3 eV) in Fig. 9(a) and S $2p_{1/2}$ (162.4, 162.0 eV) in Fig. S8). After assembling CdS with NYF, the binding energies of S $2p_{1/2}$ in CdS/NYF and Pt/CdS/NYF appear red shift from 162.4 to 162.1 and 162.0 eV respectively. The binding energies of Na 1 s present blue shift from 1071.6 to 1071.8 and 1071.9 in NYF, CdS/NYF and Pt/CdS/NYF. That means that there are strong interactions between CdS and NYF via the heterojunction. This charge density shift might form an inner electric field between CdS and NYF and result in the easy charge transfer from CdS to NYF, which preferred the promotion of stability of Pt/CdS/NYF. There were no obvious chemical state changes of Cd, S, Na, Er, Yb and Pt in Pt/CdS/NYF photocatalyst before and after reaction (Fig. S9), indicating catalyst was stable during reaction.

The fluorescence lifetimes over CdS, CdS/NYF and Pt/CdS/NYF are also shown in Table 1. These data are obtained by fitting the decay profiles with two exponential terms. The average charge lifetimes in the presence of NYF increase remarkably, which illustrate that the NYF and Pt on Pt/CdS/NYF effectively reduce the recombination of electron-hole and prolong the lifetime of photoexcited charges.

3.4. The mechanism of water splitting over Pt/CdS/NYF photocatalyst

Based on all the experimental results shown above, we illustrate the mechanism of water splitting over Pt/CdS/NYF in Scheme 2. Firstly, the NYF captures NIR light and up-converts visible light to CdS through UC process to generate charges. The CdS is n-type semiconductor with electrons as the majority carriers and the bandgap is about 2.2 eV (Fig. (S10)). Accordingly, the flat band position of CdS matches the energy level of the NYF (Fig. 10). Specifically, The levels of Yb^{3+} and Er^{3+} ions in NYF (E_0, E_1, E_2) permit the up-conversion process taking placing by the absorption of sub-bandgap (causing by Yb^{3+} and Er^{3+}) photon (ω_1, i.e., the NIR light absorbed by Yb^{3+}), the excited intermediate state accepted second photon (ω_2, another photon absorbed by Er^{3+}) jumping to higher energy level, eventually emitting higher energy photons (ω) was formed by de-excitation to the ground state energy level (e.g., emitting red light by $^4F_{9/2} \rightarrow {}^4I_{15/2}$ process). As a results, NIR light is up-converted into visible light [56–58] which was used by CdS to catalyse hydrogen evolution under NIR light irradiation. By taking advantage of the inner electric field between CdS and NYF, the charge transfer between CdS and NYF became smoothly. The overall water splitting to hydrogen and oxygen under NIR irradiation is achieved.

4. Conclusions

In summary, overall water splitting under NIR light irradiation has been successfully achieved by assembling CdS with the NIR-to-visible UC component NYF. The NIR-to-visible UC units in photocatalysts up-converted the incident NIR radiation to visible light emission, the emitted visible light can be used by CdS to form excited charges. Owing to the heterojunctions constructed between the NIR-to-visible UC unit and visible-responsive CdS, the overall water splitting has been achieved. The highest hydrogen evolution rate is 3.38 μmol g^{-1} h^{-1} under 980 nm irradiation. This study inspires the utilization of visible-responsive materials to realize overall split water by NIR light irradiation of sun irradiation.

Acknowledgement

This work was financially supported by the China National Key

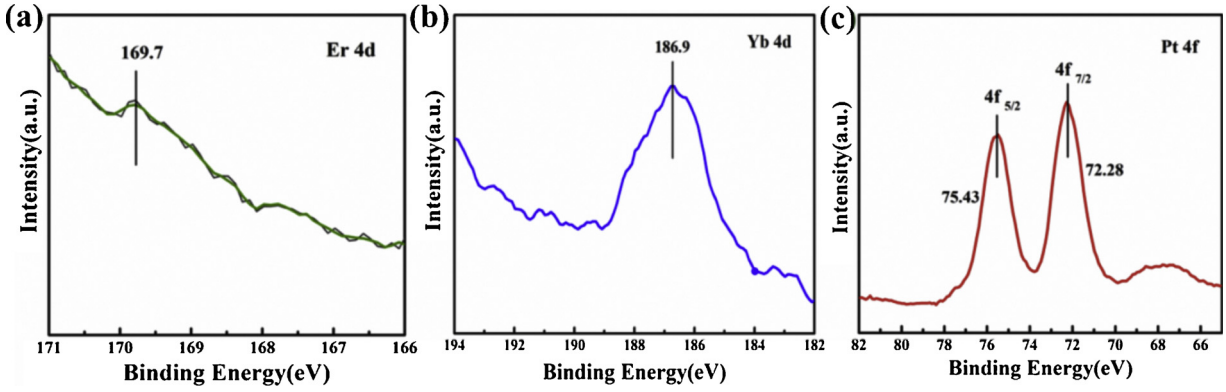

Fig. 8. XPS spectra of (a) Er, (b) Yb and (c) Pt elements.

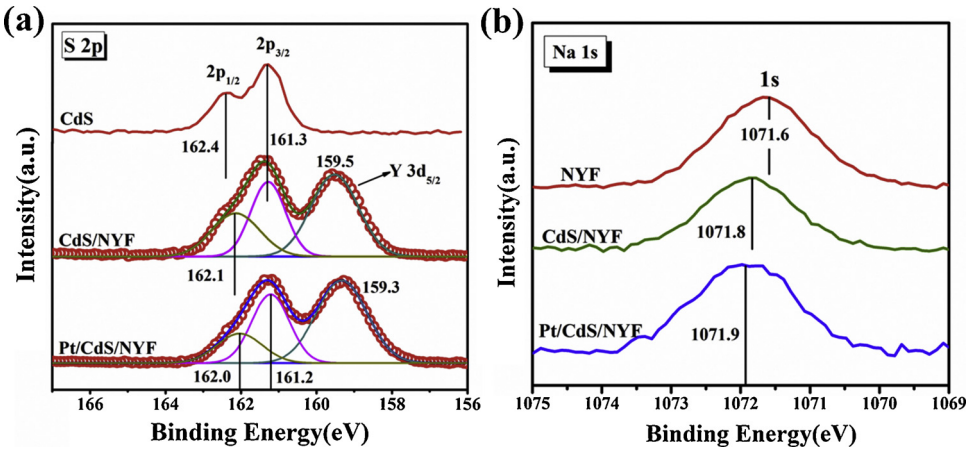

Fig. 9. XPS spectra of (a) S 2p and (b) Na 1s.

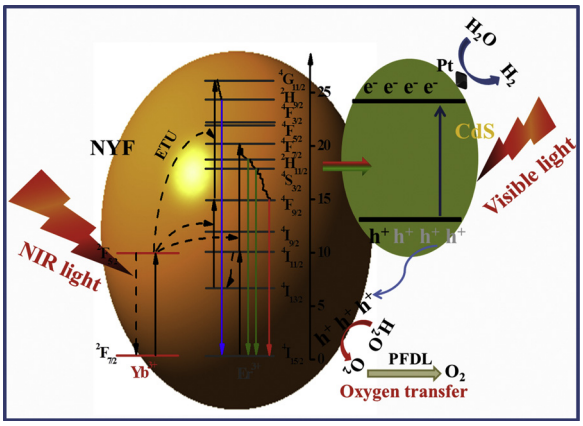

Scheme 2. NIR/Visible-light-driven overall water split over Pt/CdS/NYF system.

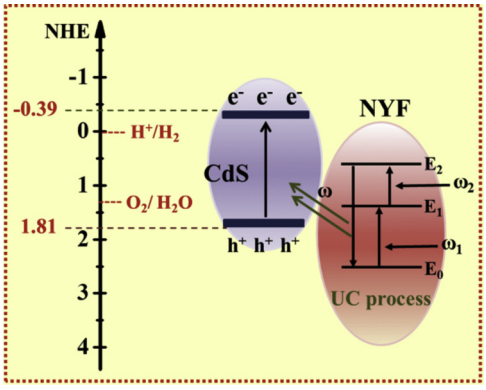

Fig. 10. Band positions of CdS and NYF.

Research and Development Plan Project (No. 2018YFB1502000) and the NSF of China (21433007, 21673262).

Appendix A. Supplementary data

Supplementary material related to this article can be found, in the online version, at doi:https://doi.org/10.1016/j.apcatb.2019.117908.

References

[1] M.S. Dresselhaus, I.L. Thomas, Nature 414 (2001) 332–337.
[2] G.X. Lu, W.Y. Zhang, J. Mol. Catal. (China) 31 (2017) 410–410.
[3] Z.X. Huang, Y.F. Li, Y.X. Li, S.Q. Peng, J. Mol. Catal. (China) 31 (2017) 181–187.
[4] R.D. Cortright, R.R. Davda, J.A. Dumesic, Nature 418 (2002) 964–967.
[5] Y.F. Zhao, R.X. Mu, P.P. Jiang, Y.M. Dong, J. Mol. Catal. (China) 32 (2018) 142–151.
[6] G.X. Lu, B. Tian, J. Mol. Catal. (China) 31 (2017) 101–104.
[7] J. Tian, Y. Sang, G. Yu, H. Jiang, X. Mu, H. Liu, Adv. Mater. 25 (2013) 5075–5080.
[8] Y.L. Zhou, L. Li, C.L. Yang, Y.Z. Jiao, X.R. Zhang, J. Mol. Catal. (China) 31 (2017) 236–246.
[9] G.X. Lu, W.L. Zhen, J. Mol. Catal. (China) 31 (2017) 299–304.
[10] Y. Deepak, B. Rangan, Renew. Sust. Energ. Rev. 54 (2016) 497–532.
[11] S.Z. Baykara, Int. J. Hydrogen Energy 29 (2004) 1459–1469.
[12] H. Ohya, M. Yatabe, M. Aihara, Y. Negishi, T. Takeuchi, Int. J. Hydrogen Energy 27 (2002) 369–376.
[13] M. Ducarroir, M. Eoex, F. Sibieude, Int. J. Hydrogen Energy 2 (1977) 251–257.
[14] T. Shari, X. Zhang, G. Costin, S. Yazdi, C.F. Woellner, Y. Liu, C.S. Tiwary, P. Ajayan, Nano Lett. 17 (2017) 7908–7913.
[15] Z.Q. Liu, X.H. Cao, B. Wang, M. Xia, S. Lin, Z.H. Guo, X.M. Zhang, S.Y. Gao, J. Power Sources 342 (2017) 452–459.
[16] X.Y. Guo, W.H. Di, C.F. Chen, C.X. Liu, X. Wang, W.P. Qin, Dalton Trans. 43 (2014) 1048–1054.
[17] W.H. Feng, L.L. Zhang, Y. Zhang, Y. Yang, Z.B. Fang, B. Wang, S.Y. Zhang, P. Liu, J. Mater. Chem. A 5 (2017) 10311–10320.
[18] J.H. Yang, D. Wang, H.X. Han, C. Li, Acc. Chem. Res. 46 (2013) 1900–1909.
[19] J.R. Ran, J. Zhang, J.G. Yu, M. Jaroniecc, S.Z. Qiao, Chem. Soc. Rev. 43 (2014) 7787–7812.
[20] K. Maeda, K. Teramura, D.L. Lu, N. Saito, Y. Inoue, K. Domen, Angew. Chem. Int. Ed. 45 (2006) 7806–7809.
[21] Q. Li, B. Guo, J. Yu, J. Ran, B. Zhang, H. Yan, J.R. Gong, J. Am. Chem. Soc. 133 (2011) 10878–10884.
[22] C. Kong, S. Min, G. Lu, ACS Catal. 4 (2014) 2763–2769.
[23] R. Abe, M. Higashi, K. Domen, J. Am. Chem. Soc. 132 (2010) 11828–11829.
[24] H.J. Li, Y. Zhou, W.G. Tu, J.H. Ye, Z.G. Zou, Adv. Funct. Mater. 25 (2015) 998–1013.
[25] M. Xu, L. Han, S.J. Dong, Appl. Mater. Interfaces 5 (2013) 12533–12540.
[26] J.F. Suyver, J. Grimm, K.W. Krämer, H.U. Güdel, J. Lumin. 114 (2005) 53–59.
[27] C. Renero-Lecuna, R. Martín-Rodríguez, R. Valiente, Chem. Mater. 23 (2011) 3442–3448.
[28] J.F. Suyver, J. Grimm, K.W. Kramer, H.U. Güdel, J. Lumin. 114 (2005) 53–59.
[29] P.P. Fang, Y.S. Pan, H. Ye, RSC Adv. 8 (2018) 35306–35313.
[30] M.J. Tou, Y.Y. Mei, S. Bai, Z.G. Luo, Y. Zhang, Z.Q. Li, Nanoscale 8 (2016) 553–562.
[31] R. Balaji, S. Kumar, K.L. Reddy, V. Sharma, K. Bhattacharyya, V. Krishnan, J. Alloys. Compd. 724 (2017) 481–491.
[32] H.F. Shi, Y.C. Yu, Y. Zhang, X.J. Feng, X.Y. Zhao, H.Q. Tan, S.U. Khan, Y.G. Li, E.B. Wang, Appl. Catal. B 221 (2018) 280–289.
[33] W. Chen, H. Liu, X. Li, S. Liu, L. Gao, L. Mao, Z. Fan, Appl. Catal. B: Environ. 192 (2016) 145–151.
[34] S.A. Rawool, M.R. Pai, A.M. Banerjee, A. Arya, R.S. Ningthoujam, R. Tewari, R. Rao, B. Chalke, P. Ayyub, A.K. Tripathi, S.R. Bharadwaj, Appl. Catal. B 221 (2018) 443–458.
[35] M. Faisal, F.A. Harraz, A.A. Ismail, A.M. El-Toni, S.A. Al-Sayari, A. Al-Hajry, M.S. Al-Assiri, Sep. Purif. Technol. 190 (2018) 33–44.
[36] J. Ng, S. Xu, X. Zhang, H. Yang, D. Sun, Adv. Funct. Mater. 20 (2010) 4287–4294.
[37] K. Iwashina, A. Iwase, Y.H. Ng, A. Rose, A. Kudo, J. Am. Chem. Soc. 137 (2015) 604–607.
[38] W. Zhu, X. Yue, W. Zhang, S. Yu, Y. Zhang, J. Wang, J. Wang, Chem. Commun. (Camb.) 52 (2016) 1486–1489.
[39] J. Wang, H. Zhong, Z. Wang, F. Meng, X. Zhang, ACS Nano 10 (2016) 2342–2348.
[40] K. Maeda, T. Takata, M. Hara, N. Saito, Y. Inoue, H. Kobayashi, K. Domen, J. Am. Chem. Soc. 127 (2005) 8286–8287.
[41] R. Abe, M. Higashi, K. Domen, J. Am. Chem. Soc. 132 (2010) 11828–11829.
[42] M. Higashi, K. Domen, R. Abe, Energy Environ. Sci. 4 (2011) 4138–4147.

[43] M. Wang, W.L. Zhen, B. Tian, J.T. M, G.X. Lu, Appl. Catal. B: Environ. 236 (2018) 240–252.
[44] E. Lalik, A. Drelinkiewicz, R. Kosydar, R. Tokarz-Sobieraj, M. Witko, T. Szumełda, J. Gurgul, D. Duraczy´nska, Appl. Catal. A Gen. 517 (2016) 196–210.
[45] X. Ning, J. Li, B. Yang, W. Zhen, Z. Li, B. Tian, G. Lu, Appl. Catal. B: Environ. 212 (2017) 129–139.
[46] T. Takata, C. Pan, M. Nakabayashi, N. Shibata, K. Domen, J. Am. Chem. Soc. 137 (2015) 9627–9634.
[47] Z. Li, B. Tian, W.L. Zhen, Y.Q. Wu, G.X. Lu, Appl. Catal. B 203 (2017) 408–415.
[48] B. Tian, W. Gao, X.Q. Zhang, Y.Q. Wu, G.X. Lu, Appl. Catal. B 221 (2018) 618–625.
[49] X.F. Ning, J. Li, B.J. Yang, W.L. Zhen, Z. Li, B. Tian, G.X. Lu, Appl. Catal. B 212 (2017) 129–139.
[50] W. Gao, W.Y. Zhang, B. Tian, W.L. Zhen, Y.Q. Wu, X.Q. Zhang, G.X. Lu, Appl. Catal. B 224 (2018) 553–562.
[51] X. Wang, J. Zhuang, Q. Peng, Y.D. Li, Nature 437 (2005) 121–124.
[52] Y.X. Li, Y.F. Hu, S.Q. Peng, G.X. Lu, S.B. Li, J. Phys. Chem. C 113 (2009) 9352–9358.
[53] Y.H. Zhang, N. Zhang, Z.R. Tang, Y.J. Xu, Chem. Sci. 3 (2012) 2812–2822.
[54] S.S. Mali, S.K. Desai, D.S. Dalavi, C.A. Betty, P.N. Bhosale, P.S. Patil, Photochem. Photobiol. Sci. 10 (2011) 1652–1658.
[55] Y. Uwamino, A. Tsuge, T. Ishizuka, H. Yamatera, Bull. Chem. Soc. Jpn. 59 (1986) 2263–2267.
[56] Z.Q. Li, X.D. Li, Q.Q. Liu, X.H. Chen, Z. Sun, C. Liu, X.J. Ye, Nanotechnology 23 (2012) 025402–025410.
[57] J. Liao, Z. Yang, H. Wu, D. Yan, J. Qiu, Z. Song, Y. Yang, D. Zhou, Z. Yin, J. Mater. Chem. C 1 (2013) 6541–6546.
[58] J. Liao, Z. Yang, S. Lai, B. Shao, J. Li, J. Qiu, Z. Song, Y. Yang, J. Phys. Chem. C 118 (2014) 17992–17999.